Comparison of Ion Irradiation Effects in PM-HIP and Forged Alloy 625

Caleb Clement<sup>1\*</sup>, Yangyang Zhao<sup>1</sup>, Patrick Warren<sup>1</sup>, Xiang Liu<sup>2</sup>, Sichuang Xue<sup>3</sup> David W.

Gandy<sup>4</sup>, Janelle P. Wharry<sup>1</sup>

<sup>1</sup> Purdue University

<sup>2</sup> Zhejiang University

<sup>3</sup> Pacific Northwest National Laboratory

<sup>4</sup> Electric Power Research Institute

\* Corresponding Author

Name: Caleb Clement

Email: clemen45@purdue.edu

Mailing Address: 205 Gates Rd, West Lafayette IN 47906

**Phone:** 865-250-0722

Keywords: PM-HIP, Powder Metallurgy, Ion Irradiation, Nanoindentation, Electron

Microscopy, Alloy 625, Ni-base Superalloys, Advanced Manufacturing

**Abstract:** The nuclear industry has growing interest in replacing forgings with structural

components fabricated by powder metallurgy with hot isostatic pressing (PM-HIP), owing to

their chemical homogeneity, uniform grain structure, and near-net shape production. This study

compares the ion irradiation response of PM-HIP and forged Alloy 625, over 50 and 100 dpa,

1

400°C and 500°C. Microstructure is characterized using down-zone bright-field scanning transmission electron microscopy (DZBFSTEM), and hardening is characterized using nanoindentation. PM-HIP Alloy 625 has a lower initial dislocation line density, resulting in a more rapid onset of dislocation loop growth and unfaulting than the forged material. But the total defect population (i.e. loop line length plus dislocation density) is insensitive to fabrication method. This finding shows promise for the eventual qualification of PM-HIP alloys for nuclear applications.

### 1.0 Introduction

Structural alloy components of nuclear power reactors have been fabricated by casting or forging for more than 60 years. But the recent emergence of advanced manufacturing methods – which can offer enhanced properties, performance, and/or economics over conventional methods - has generated substantial interest in considering these new technologies for use in existing and future next-generation nuclear power applications[1]. Powder-based manufacturing technologies are amongst the most mature methods being investigated, including powder metallurgy with hot isostatic pressing (PM-HIP) [2,3]. PM-HIP leverages a solid-state diffusion process to achieve densification of gas atomized metallic powders at isostatic pressures in excess of 100 MPa and temperatures at or above 0.7T<sub>m</sub> [4,5]. As compared to conventional code-qualified fabrication methods such as casting and forging, PM-HIP produces components with higher density, greater chemical homogeneity, uniform and equiaxed grain structure, fewer defects, and exceptional mechanical properties. Additionally, PM-HIP products can be produced near-net shape, which reduces the need for welding and machining post fabrication [2,3,6]. Beyond powder metallurgy, HIP alone has long been used as a post-processing treatment to densify as-cast metals and can be used to relieve dendritic grain structures in additively manufactured materials [7,8].

Ongoing efforts aim to generate qualification data for a variety of PM-HIP nuclear structural alloys, including austenitic and ferritic steels and Ni-base alloys[9] But thus far, irradiation effects on PM-HIP alloys have not yet been widely studied. Bergenlid and Lind conducted tensile and creep tests on PM-HIP 316LN stainless steel irradiated to 0.7 dpa with neutrons, and found that the PM-HIP steel had a higher degree of hardening than its wrought counterpart, with similar reductions in ductility [10]. Jiang *et al.* [11] studied void swelling in additively manufactured 316L treated with HIP and ion irradiated up to 100 dpa at varying

temperatures; the HIP condition displayed a delayed onset of void swelling as compared to its non-HIP counterpart [11]. These reports present inconclusive and somewhat contradictory findings on the irradiated microstructure and mechanical properties of PM-HIP alloys, thus warranting further investigation.

The present study focuses on PM-HIP Alloy 625, which is a Ni-base superalloy solution strengthened by Nb and Mo; under long-term thermal aging, it can also be precipitation hardened by a homogenous dispersion of  $\gamma$ " phase [12,13]. Ni-base superalloys including Alloy 625 are of particular interest for in-core structural components in Generation IV nuclear reactor systems such as molten salt reactors (MSR) and the gas-cooled very high temperature reactor (VHTR) [14,15]. In such applications, Ni-base alloy components will operate at temperatures up to ~600-700°C and irradiation fluences ~10s-100s of displacements per atom (dpa). In the existing fleet of light water nuclear reactors (LWRs), Alloy 625 is used for applications such as heat exchanger tubing, steam generators, pipes, and valves, due to its high temperature strength and corrosion resistance [16–18].

The irradiation response of Alloy 625 is also not clearly understood, with limited and inconclusive reports; additionally, the effect of processing method has not yet been addressed. Yu and Marquis irradiated Alloy 625 to 1.5 dpa at 300°C with 5 MeV Ni ions, and found irradiation induced ballistic dissolution of pre-existing  $\gamma$ " phases [18]. Song et al. conducted proton irradiation on Alloy 625 using 2 MeV protons at 360°C to 2.5 dpa, and observed long-range ordering [19]. A variety of mechanical behaviors is also observed, dependent on the irradiation temperature. For example, Cieslik et al. [20] irradiated additively manufactured Alloy 625 to 1 dpa at room temperature with 1.6 MeV Ni ions; they attributed irradiation hardening to

dislocation loop formation. But Bajaj et al. irradiated Alloy 625 with neutrons to a fluence of  $2.3 \times 10^{20} \text{n/cm}^2$  at 360°C, and observed irradiation softening with an increase in elongation [21].

The objective of the present study is to understand the effects of ion irradiation on the microstructural evolution and mechanical properties of Alloy 625 manufactured by PM-HIP compared to forging. The identical PM-HIP ingots studied herein have already shown promising mechanical performance compared to the identical forged ingots, in the as-fabricated condition and after isothermal aging. Guillen et al. conducted in situ tensile studies using high energy Xray diffraction [22], and observed PM-HIP Alloy 625 to have superior yield and tensile strength, and more homogeneous grain-level stress distribution, compared to forged Alloy 625. After isothermal aging at up to 800°C for up to 1000 hr, both Bullens et al. and Getto et al. reported comparable hardening and grain size stability in forged and PM-HIP Alloy 625 [13,23]. In the present study, ion irradiation will be conducted on the same PM-HIP and forged Alloy 625 ingots, to doses of 50 and 100 dpa at irradiation temperatures of 400°C and 500°C. The irradiated microstructure will be characterized to reveal the dependence on irradiation dose and temperature. Nanoindentation will be used to correlate microstructure evolution with hardness. This study is the first of its kind to directly compare the irradiation response of PM-HIP and forged Alloy 625; results will contribute to the broader understanding of irradiation effects in Nibase alloys.

#### 2.0 Materials and Methods

### 2.1 Fabrication and Irradiation

Ingots of PM-HIP and forged Alloy 625 were furnished by the Electric Power Research Institute (EPRI). To fabricate the PM-HIP ingot, gas atomized Alloy 625 powders were mixed

and filled into a canister that was sealed and then HIPed at conditions of  $1121^{\circ}$ C and 15 ksi. The forged ingot was cast and hot rolled before being subjected to an initial solution annealing at  $1040^{\circ}$ C for 2 hours and 40 minutes, followed by air cooling. After initial processing, the PM-HIP ingot was solution annealed at  $1171^{\circ}$ C for 2 hours followed by water quenching, while the forged ingot was given a two-step heat treatment of solution annealing at  $1075^{\circ}$ C for 30 minutes followed by water quenching, then thermal aging at  $700^{\circ}$ C for 15 hours followed by air cooling [13]. Both ingots were fabricated in order to produce mechanical properties compliant with ASME boiler pressure-vessel code (BPVC); the heat treatments were not intended to produce  $\gamma''$  precipitation [24]. The nominal elemental compositions were measured by inductively coupled plasma atomic emission spectroscopy (ICP-AES) for material certifications, and subsequently by the authors using energy dispersive x-ray spectroscopy (EDS) in a scanning electron microscope (SEM), as detailed in Table 1.

The ingots were sectioned into 2 x 2 x 20 mm matchsticks using electrical discharge machining (EDM). One of the 2 mm x 20 mm faces of each matchstick specimen was polished to a mirror finish using SiC paper through 1600 grit and subsequent vibratory polishing in Al<sub>2</sub>O<sub>3</sub>. Finally, specimens were electropolished at 35 V for 20 s using a Pt mesh cathode in a 90% methanol, 10% perchloric acid solution maintained at -40°C.

The polished matchstick specimens underwent ion irradiation at the Michigan Ion Beam Laboratory (MIBL) using 4.5 MeV Fe<sup>++</sup> ions. The damage profile was predicted using Stopping Range of Ions in Matter (SRIM) 2013 software [25,26] in the "Quick Calculation" Kinchin-Pease mode with displacement energies of 40 eV [20,26–28]. The challenges of characterizing the irradiated microstructure in ion irradiated layers with steep damage gradients have been well documented [29]: the near-surface region was affected by the surface sink as well as effects such

as sputtering, while the irradiation damage peak region was affected by proximity to the ion implantation peak. Hence, the target depth of interest for microstructural evaluation was located at a depth of 400-700 nm from the surface, Figure 1. All further microstructure analyses and references to irradiation dose (i.e. dpa) levels in this manuscript correspond to this depth of interest. All specimens were irradiated at  $400 \pm 10^{\circ}$ C and  $500 \pm 10^{\circ}$ C to a target depth range dose of 50 and 100 dpa at dose rates ranging from  $7.41 \times 10^{-4}$  to  $1.18 \times 10^{-3}$  dpa/s, as summarized in Table 2. Note, however that the  $500^{\circ}$ C 50 dpa irradiation condition was only conducted on the PM-HIP alloy.

### 2.2 Microstructural Characterization

Irradiated and as-received microstructure characterization focused on dislocation networks, dislocation loops, and voids (if present), using transmission electron microscopy (TEM). Cross-sectional TEM lamellae were created from each specimen condition using the focused ion beam (FIB) lift-out method [30,31]. Lamellae locations were selected to cross one or more grain boundaries in order to increase the likelihood of locating a grain oriented close to a low-index zone axis for subsequent microstructure characterization. A  $20 \times 1.5 \times 2\mu m$  Pt cap was deposited, and then bulk milling was performed using  $Ga^+$  ions at 30 kV and 7 nA current. The lamellae were then Pt-welded to a Cu TEM half-grid. The as-mounted dimensions of the lamellae were approximately  $20 \times 7 \times 2 \mu m$ . The lamellae were then thinned to <100 nm using  $Ga^+$  ions at 30 kV and 1 nA current, by alternating thinning on either side of the lamella at  $\pm 1.5^\circ$  tilt. The lamellae were given a final polish at 5 kV before the ion voltage was reduced to 2 kV to remove FIB damage from the surfaces of the lamellae. Thermo Scientific (previously FEI)

Quanta 3D FEG and Helios G4 UX dual-beam FIB/SEMs at Purdue University were used for all FIB work.

TEMs used in this work were a Thermo Scientific (formerly FEI) Tecnai TF30-FEG TEM/STEM at the Center for Advanced Energy Studies (CAES), as well as a Thermo Scientific Tecnai T20, Talos 200X, and Themis Z at Purdue University. The Tecnai TEMs were principally used for bright field imaging and identification of zone axes, while the Talos and Themis TEMs were used for scanning TEM (STEM) and dislocation imaging. Dislocation loops were imaged using the down-zone axis annular bright field STEM (DZBFSTEM) technique described by Parish et al. [32]. Throughout this investigation, all DZBFSTEM images were taken along the [110] zone axis. Contrary to traditional loop imaging in the two-beam condition, which only allows imaging of dislocation loops that exactly satisfy the diffraction conditions, or the dark field rel-rod technique, which only reveals edge-on dislocation loops, DZBFSTEM relaxes the g•b invisibility criterion and images all loop orientations simultaneously. This technique allows for faster characterization with strong contrast as compared to traditional methods, as well as high statistical accuracy [33,34]. Recent work by Xiu et al. illuminates the orientation of faulted and perfect loops at each low-index zone axis for FCC materials [35]. The through-focus technique in bright field TEM was used to check for the presence of voids. Composition was determined by TEM energy dispersive x-ray spectroscopy (EDS). Lamella thickness was determined using electron energy loss spectroscopy (EELS). The STEM and TEM data was analyzed using Gatan Digital Micrograph and TEM Instrument Analysis (TIA) software.

## 2.3 Nanoindentation

Nanoindentation was performed on the as-received and irradiated specimens in order to gain an understanding into the irradiation-induced hardening. A KLA (formerly Nanomechanics) iMicro nanonindenter was used to make indents on each specimen condition. The nanoindenter was installed with a Berkovich tip, and the tests were performed using continuous stiffness mode (CSM) in depth-controlled indentation to a maximum depth of 3500 nm with an applied strain rate of 0.2 s<sup>-2</sup>. For each condition, an array of at least 40 indentations were performed in a topdown manner, in the direction of irradiation, as illustrated in Figure 1. Due to specimen mounting constraints, the PM-HIP 500 °C 100 dpa specimen was indented cross-sectionally rather than top-down; these indents were positioned 400-700 nm from the edge (i.e. irradiated surface) to correspond with the target depth range of interest. A total of 16 cross-sectional indents were made on the PM-HIP 500 °C 100 dpa specimen to a depth of 1000 nm with an applied strain rate of 0.2 s<sup>-2</sup>. The plastic zone of the indentation extends almost 5 times deeper into the specimen than the indent depth [36–40]. This would mean indentations to probe hardening in the target depth for dose and microstructure evaluation would have to be ~100-200 nm deep and as such, would be affected by surface roughness and indentation size effects (ISE) [41–43]. Therefore, top-down indents will be used in this study as a qualitative means of assessing hardening in the irradiated specimens.

#### 3.0 Results

### 3.1 As-Received Microstructure

The as-received grain microstructures for both the forged and PM-HIP materials have been previously investigated, and the average grain sizes are  $9.0 \pm 8.2~\mu m$  and  $6.9 \pm 10~\mu m$ 

respectively [13,22]. Corresponding EBSD maps of the as-received grain microstructure are shown in the supplementary information file.

Fig. 2 illustrates the difference in initial dislocation microstructure between the forged and PM-HIP specimens. The forged specimen has an initial dislocation density of 0.85 x 10<sup>14</sup> m<sup>-2</sup>, which is five times that in the PM-HIP specimen, 0.16 x 10<sup>14</sup> m<sup>-2</sup>, Table 3. These dislocation densities are an order of magnitude lower than that observed in cold worked Alloy 625 from Gao et al. [44]. Since HIP is often used as a post-processing treatment to reduce porosity and alleviate dislocation pile-up in metallic alloys [45,46], it is reasonable for the PM-HIP specimen to have a lower initial dislocation density than the forged specimen. It is also possible that a lower solution annealing temperature for the forged specimen contributed to a higher initial dislocation density.

Both alloy fabrication conditions exhibit micro-scale (Nb,Mo)-rich carbide formation at grain boundaries as indicated by the yellow arrows in Fig. 2a and 2b; their compositions are confirmed by EDS and is provided in the supplementary information file. Getto et al. also observed formation of these carbides in specimens taken from the same forged and PM-HIP ingots, during the initial heat treatment [13]. These (Nb,Mo)-rich carbides are considered secondary carbides. However, the primary strengthening phase  $\gamma$ " that precipitates under specific conditions in some Ni-based alloys, is not observed in either the forged or PM-HIP specimen. Diffraction patterns in Fig. 2 show no superlattice spots associated with the presence of  $\gamma$ ". Yu and Marquis heat treated Alloy 625 at 650°C, and do not observe formation of  $\gamma$ " until after 25 hours, so a lack of  $\gamma$ " in this study is reasonable given the heat treatment conditions employed [12,18]. Additionally, in the PM-HIP specimen, Al-rich oxide precipitates having diameters ~10s-100s of nm, are observed and indicated using red arrows in Fig. 2b. The presence of oxides has also been confirmed in PM-HIP Alloy 625 studied by Berglund and Meurling, as

well as Sergi et al. [47,48]. Because both the carbide and oxide precipitates are present at a relatively low number density, their population within the 400-700 nm depth of interest in a cross-sectional ion irradiated TEM lamella is statistically insignificant. Hence, these precipitates will not be characterized in the irradiated specimens.

### 3.2 Irradiated Microstructure Evolution

Dislocation loops nucleate homogenously under irradiation in all specimen conditions. Representative micrographs of the dislocation loop and line microstructure at each irradiation condition can be seen in Fig. 3. Loop size, loop number density, Frank loop fraction, and dislocation density are quantified in Table 3. In all irradiated specimen conditions examined, average loop diameters fall into a narrow range ~8-14 nm at number densities ~10<sup>21</sup>-10<sup>22</sup> m<sup>-3</sup>, with dislocation line densities ~10<sup>14</sup> m<sup>-2</sup>. Studies performed on alloy 625 irradiated with protons [16,49–52], neutrons [21] and ions [18] show comparable values for loop size and number density.

Mean dislocation loop sizes and number densities (Fig. 4, Table 4) are statistically equivalent at 400°C between the PM-HIP and forged specimen, although at 500°C, the forged specimen has larger loops at a lower number density than the PM-HIP specimen. The dose dependence of loops is complex. At 500°C, the PM-HIP alloy dislocation loop size and number density increase with increasing dose from 50 to 100 dpa. But at 400°C, both alloys exhibit decreasing loop size and increasing loop density with increasing dose. Such a decrease in loop diameter with increasing dose in a high-dose (i.e. >10 dpa) regime has been previously observed by Ulmer et al. in heavy-ion irradiated alloy 800H [53]. Temperature has little effect on loop size in PM-HIP Alloy 625, although in the forged specimen, average loop size increases with

temperature. In both alloys, loop number density decreases with increasing temperature from 400°C to 500°C. Loop growth and reduction in number density is typical in irradiated Ni-base alloys with increasing temperature [33,54,55]. Dislocation loop size distribution histograms for all irradiation conditions (Fig. 5) confirm that loop sizes increase with irradiation temperature, and that this trend is considerably more pronounced in the forged alloy than the PM-HIP alloy.

It is well known that in Alloy 625 and other f.c.c. Ni-based alloys and superalloys, irradiation nucleates both faulted (Frank) dislocation loops with  $\vec{b} = \frac{a}{3} < 111 >$  and perfect dislocation loops with  $\vec{b} = \frac{a}{2} < 110 > [56,57]$ . The fraction of the total dislocation loop microstructure identified as Frank loops ranges between 0.45 and 0.60 in all conditions, Table 4. The formation and stability of faulted Frank loops are strongly influenced by the stacking fault energy. Because stacking fault energy decreases with increasing chemical complexity [58,59], engineering alloys should have a higher fraction of Frank loops than laboratory-purity model alloys. Indeed, Xiu et al. [33]irradiated model Ni-20Fe and NiFe-20Cr, and found the Frank loop fraction at 7.2 dpa to be 0.078 and 0.188, respectively.

Irradiation causes the dislocation density to increase by an order of magnitude across all specimen conditions (Fig. 6, Table 4). Dislocation line density appears relatively insensitive to irradiation temperature. At 400°C, dislocation line density increases in the forged alloy from 50 to 100 dpa, but is statistically unchanged in the PM-HIP alloy. At 500°C, PM-HIP dislocation line density decreases from 50 to 100 dpa.

The total line density (Fig. 4b) considers the total dislocation loop line length  $(N_{avg} \times d_{avg})$  and the dislocation line density. The total line density of the forged and PM-HIP alloys are statistically equivalent at each irradiation condition. At 400°C, both the forged and PM-HIP total line densities increase from 50 to 100 dpa, but at 500°C, the total line density in the

PM-HIP specimen appears to saturate by 50 dpa. Additionally, the total line density decreases in both specimens with increasing temperature, which is consistent with other studies of Ni-base alloys [54,55,60].

Irradiation-induced voids are not observed in any of the specimen conditions.

Representative through-focus images for forged and PM-HIP specimens can be found in the supplementary information file. This lack of voids is unsurprising because the absence or limitation of void formation during ion irradiation without dual helium implantation at intermediate temperatures has been well documented in the literature [49,55,60–64].

# 3.3 Mechanical Properties

Nanoindentation hardness-depth profiles (Fig. 6) are averaged over all 40+ nanoindentations made on a given specimen condition. In the as-received forged and PM-HIP specimens, surface size effects are overcome by depths <400 nm, and bulk hardness values are 3.99 GPa and 4.05 GPa respectively. In the ion irradiated specimens, the near-surface peak hardness exhibits an extended shoulder over depths ~300-800 nm associated with the irradiation hardening phenomenon [57] due to the irradiation damage and ion implantation profiles. The relative magnitudes of these shoulders can be used to qualitatively evaluate the extent of irradiation hardening within the target dose and microstructure analysis depth region. This can be more clearly resolved by plotting the square of hardness against the inverse of the indent depth (insets, Fig. 6). Changes in slope along the H<sup>2</sup> vs. 1/h curves are indicative of different regions along the hardness-depth profile. Specifically, a slope change near  $1/h \sim 0.003$  reveals the overcoming of surface effects, while a slope change near  $1/h \sim 0.001$  is indicative of

indenting beyond the irradiation damage peak. The region between these two slope changes reveals the hardness at corresponding depths along the irradiation damage profile.

Both the PM-HIP and forged alloys exhibit greater irradiation hardening at 400°C than at 500°C. This follows the trend that irradiation-induced hardening decreases with increasing temperature, as shown in several solution annealed Ni-base alloys including C-276 irradiated at 300°C and 500°C [55], Alloy 706 irradiated at 450°C and 500°C [65], and a model NiFe-20Cr irradiated to 38.4 dpa at 500°C and 580°C [33].

At 400°C, the forged alloy hardens between 50 and 100 dpa, while the PM-HIP specimen does not exhibit an appreciable increase in hardening from 50 to 100 dpa. This indicates a potential saturation in irradiation hardening for the PM-HIP specimen that occurs around or before 50 dpa, while the forged specimen does not saturate until above 50 dpa. Recall that the cross-sectional nanoindentation hardness-depth profile on the 500°C 100 dpa PM-HIP specimen (marked \* in Fig. 6b) is not directly comparable to the other hardness-depth profiles but nevertheless confirms the presence of irradiation hardening at this specimen condition. High-dose saturation of irradiation hardening is expected in Ni-based alloys and austenitic stainless steels [33,66].

### 4.0 Discussion

### 4.1 Loop Unfaulting

The irradiation-induced increase in dislocation density in both alloys may be attributed to Frank loops unfaulting into perfect loops, as indicated by the decreasing Frank loop fraction with increasing dose (Table 4). Xiu et al. also observed a decrease in the fraction of Frank loops compared to perfect loops while Frank loop size increased for NiFe-20Cr irradiated to 7.2 dpa

and 38.4 dpa respectively at both 500°C and 580°C [33]. This lends credence to the idea that larger Frank loops are more susceptible to unfaulting because larger loops are more likely to interact with perfect loops and network dislocations in the microstructure as those glissile features move. Loop unfaulting is a well understood step in the dislocation loop evolution cycle and occurs when the loop microstructure grows enough that individual loops interact with each other and with network dislocations [67]. The loop unfaulting process has been described by Gelles and has been documented in other Ni-based alloys under irradiation [54,60,68,69]. In this mechanism, the sessile a/3 <111> Frank loop interacts with an a/2 <110> perfect dislocation to form a Shockley partial dislocation in the reaction:

$$\frac{a}{3}[111] + \frac{a}{2}[\bar{1}\bar{1}0] = \frac{a}{6}[\bar{1}\bar{1}2] \tag{1}$$

This Shockley partial sweeps across the front of the faulted loop, removes the stacking fault, and reacts with the back side of the loop to form a glissile perfect loop. This perfect loop goes on to glide and impinge with other loops, adding to the dislocation network following the reaction:

$$\frac{a}{6}[\overline{112}] + \frac{a}{3}[111] = \frac{a}{2}[\overline{110}] \tag{2}$$

Loop unfaulting is supported by the relative loop and network dislocation contributions to the total line density (Fig. 4b). At 500°C, network dislocations generally comprise a larger fraction of the total line density in both the PM-HIP and forged specimens than at 400°C. This occurs because with increasing temperature, defects and dislocations become more mobile, which leads to enhanced annealing and loop unfaulting. Considering now only the 100 dpa PM-HIP experiments, network dislocations contribute a lower fraction to total line density with increasing temperature, which indicates that the rate of dislocation annealing outpaces the rate of Frank loop unfaulting into the dislocation network. By contrast in the 100 dpa forged experiments, the network dislocations contribute a larger fraction to total line density with

increasing temperature, indicating that the rate of Frank loop unfaulting exceeds that of dislocation annealing. This greater extent of unfaulting in the forged specimen can be explained by the larger average loop diameter at 500°C, 100 dpa than that of its PM-HIP counterpart.

# 4.2 Role of Sink Strength in Irradiation Tolerance

The PM-HIP and forged alloys have nearly identical total line densities in all irradiated conditions (Fig. 4b), suggesting that both alloys have comparable overall defect tolerance. However, the relative contributions of loops and lines to this total line density, varies across alloys and irradiation conditions. This variability is attributed to the initial sink strengths of the PM-HIP and forged specimens, which have a significant impact on the irradiation response of Ni-base alloys [63]. The initial dislocation network, grain boundaries, and precipitates contribute to the total sink strength of the material, as summarized in Table 3; the reader is referred to the supplementary information for details of the sink strength calculation [57,70,71].

The dislocation contribution to sink strength of the as-received PM-HIP alloy is  $0.2x10^{14}$  m<sup>-2</sup>, while that of the as-received forged alloy is  $1.22x10^{14}$  m<sup>-2</sup>. Grain boundaries and precipitates are negligible, as their sink strength contributions are  $\geq 2$  orders of magnitude lower than that of dislocations. A higher initial sink strength is generally indicative of greater irradiation tolerance, since the point defects generated from the irradiation damage cascade will diffuse to sinks where they become annihilated before they are able to cluster into loops or voids [75–78]. It is therefore expected that the nearly order-of-magnitude greater sink strength of the as-received forged alloy compared to the PM-HIP alloy would make the PM-HIP alloy initially more susceptible to irradiation damage.

This enhanced susceptibility to irradiation damage can most clearly be seen in the 400°C irradiations. Although the PM-HIP and forged specimens have statistically identical dislocation loop sizes and number densities at both doses at 400°C, the PM-HIP dislocation line density is considerably higher than that of the forged specimen at 50 dpa. This suggests that the PM-HIP specimen experiences more rapid (i.e. <50 dpa) dislocation loop nucleation, growth, and subsequent unfaulting into dislocation lines than the forged specimen. This idea is further supported by the saturation in the PM-HIP dislocation density between 50 and 100 dpa at 400°C, whereas the forged specimen experiences a statistically significant increase in dislocation density between 50 and 100 dpa to saturation. While both alloys ultimately achieve a similar total line density by 100 dpa, their evolution toward that similar structure may differ based on their initial sink strengths. In other words, the higher initial sink strength of the forged specimen may delay the onset of phenomena, similar to how "radiation tolerant" microstructures do not entirely eliminate void swelling, but instead introduce a void incubation period [79,80]. Thus, the total defect population is independent of fabrication method once irradiation begins – it is only the ratio of loop to line defects that is dependent upon fabrication method (i.e. initial sink strength or dislocation density).

The initial sink strength also influences the radiation tolerance at 500°C, although the increase in thermal energy promotes Frank loop unfaulting and annealing of the network dislocations, which lowers the saturation density of the microstructures. The PM-HIP specimen again exhibits considerable loop unfaulting into dislocation lines by 50 dpa at 500°C. But unlike the dislocation saturation observed between 50 and 100 dpa at 400°C, the dislocation density decreases between 50 and 100 dpa at 500°C due to annealing. Additionally, the forged specimen at 500°C, 100 dpa has larger and less populous loops and a higher dislocation density than the

PM-HIP specimen. This again suggests that the lower initial sink strength in the PM-HIP specimen enables more rapid loop growth, while the higher initial sink strength in the forged specimen delays the onset of irradiation-induced phenomena. Both alloys again reach a similar total line density by 100 dpa.

Differences in initial solution annealing conditions between the PM-HIP and forged specimen likely contribute to the observed differences in initial dislocation structures and sink strength. Tailoring annealing conditions may produce comparable initial microstructures in both alloys that will evolve more similarly under irradiation. Additionally, the differences in composition between the PM-HIP and forged alloys are acknowledged. Minor differences in micro-alloyed elements, specifically Si and Ti, have been shown to affect loop size, morphology and number density in Ni as well as FCC multi-principal-element alloys (MPEAs) [72–74]. According to Hoffman et al. the addition of Ti decreases the stacking fault energy (SFE) of the system and stabilizes faulted Frank loops, leading to a larger diameter and lower number density of Frank loops. However, this phenomena is inconsistent with observations in the present study; rather, the major contributor to sink strength and microstructural evolution is the initial dislocation density.

### 5.0 Conclusions

PM-HIP and forged Alloy 625 are ion irradiated to 50 and 100 dpa at 400°C and 500°C. Irradiation-induced microstructural evolution is characterized, and irradiation hardening is evaluated using nanoindentation. Major conclusions are:

- The overall microstructural and mechanical irradiation response of the PM-HIP specimen
  is comparable to that of the forged specimen, offering promise for the performance of
  PM-HIP manufactured materials in nuclear systems.
- The total defect population (i.e. loops and lines) is independent of fabrication method.

  The relative populations of loops to lines is dependent upon fabrication method, by virtue of the initial sink strength. The higher initial sink strength in the forged specimen delays the onset of dislocation loop growth and unfaulting, compared to that in the PM-HIP specimen containing a lower initial sink strength. This behavior can be likened to an incubation period.
- Total line density (i.e. sum of loop line length and dislocation line density) are similar across both PM-HIP and forged alloys over all irradiation conditions, but the relative contributions of loops and lines differs based on the initial sink strength of the alloys.
- Irradiation hardening is consistent with the microstructural evolution.

### Acknowledgements

This work was supported by the Electric Power Research Institute (EPRI). Irradiation experiments and microstructure characterization was supported by the US Department of Energy – Office of Nuclear Energy, through the Nuclear Science User Facilities (NSUF) contracts 15-8242 and 18-1412. The authors thank Dr. Yaqiao Wu, Megha Dubey, and the staff at the Center for Advanced Energy Studies (CAES) for assisting with portions of the work. Additionally, the authors thank Dr. Rosa Diaz and Dr. Chris Gilpin for assistance at the Purdue Electron Microscopy Facility and Birck Nanotechnology Center.

# **Tables & Figures**

Table 1: Nominal elemental compositions (wt%) measured by ICP-AES (material certifications) and by SEM EDS.

Sample	Method	Mn	Si	Cr	Ni	Al	Mo	Fe	Nb	Ti	F	C	P	S	0
PM-HIP	Certification <sup>†</sup>	0.41	0.45	21.9	Bal	< 0.05	8.2	3.6	3.7	0.006	-	0.01	0.003	0.003	-
	SEM EDS	0.544	0.688	23.0	Bal	0.106	7.25	3.57	3.75	-	0.22	-	-	-	0.25
Forged	Certification <sup>†</sup>	0.35	0.12	21.8	Bal	0.09	8.4	3.5	3.6	0.18	-	0.01	0.006	0.004	-
	SEM EDS	0.415	0.195	23.7	Bal	0.308	7.58	3.52	3.57	0.313	1	-	-	-	-

<sup>†</sup> material certification composition also includes <0.1 Cu, <0.1 Cu, and <0.010 Pb.

Table 2: Irradiation experiment matrix.

Specimens	Temperature (°C)	Dose (dpa)	Dose Rate (dpa/s)	
PM-HIP and Forged	400	50	1.04x10 <sup>-3</sup>	
PM-HIP and Forged	400	100	1.18x10 <sup>-3</sup>	
PM-HIP only	500	50	7.41x10 <sup>-4</sup>	
PM-HIP and Forged	500	100	1.1x10 <sup>-3</sup>	

Table 3: Summary of as-received microstructure in PM-HIP and forged specimens.

Alloy	Feature	Value	Sink strength
			$(x10^{14} m^{-2})$
Forged	Grain size (x10 <sup>-6</sup> m)	9.0 ± 8.2	0.003
	Dislocation line density (x10 <sup>14</sup> m <sup>-2</sup> )	$0.85 \pm 0.13$	1.22
	Carbide size (x10 <sup>-6</sup> m)	$0.91 \pm 0.16$	
	Carbide number density (x10 <sup>17</sup> m <sup>-3</sup> )	$1.85 \pm 0.92$	0.021
PM-HIP	Grain size (x10 <sup>-6</sup> m)	6.9 ± 10	0.005
	Dislocation line density (x10 <sup>14</sup> m <sup>-2</sup> )	$0.16 \pm 0.03$	0.2
	Carbide size (x10 <sup>-6</sup> m)	$1.36 \pm 0.5$	
	Carbide number density (x10 <sup>17</sup> m <sup>-3</sup> )	2.41 ± 1.2	0.041
	Oxide size (x10 <sup>-6</sup> m)	$0.22 \pm 0.03$	

Oxide number density (x10 <sup>17</sup> m <sup>-3</sup> )	$4.34 \pm 2.2$	0.012
---	----------------	-------

Table 4: Summary of irradiation-induced dislocation loop and line microstructure evolution.

Alloy	Condition	Loop Size	Loop Number	Frank Loop	Dislocation Line
		(nm)	Density (x10 <sup>21</sup> m <sup>-</sup>	Fraction	Density (x10 <sup>14</sup> m <sup>-2</sup> )
			3)		
Forged	As-received	-	-	-	$0.85 \pm 0.13$
	400°C, 50 dpa	9.61	7.02 ± 1.05	0.58 ± 0.026	$2.27 \pm 0.1$
		<u>+</u> 0.52			
	400°C, 100 dpa	7.95	16.7 ± 2.18	0.49 ± 0.028	$3.62 \pm 0.71$
		± 0.34			
	500°C, 100 dpa	14.4	$2.38 \pm 0.08$	0.52 ± 0.018	4.57 ± 0.75
		<u>±</u> 0.79			
PM-HIP	As-received	-	-	-	$0.16 \pm 0.03$
	400°C, 50 dpa	9.78	7.55 ± 0.56	0.48 ± 0.026	$3.82 \pm 0.25$
		<u>±</u> 0.34			
	400°C, 100 dpa	8.18	12.5 ± 2.41	$0.48 \pm 0.020$	$4.32 \pm 0.73$
		<u>±</u> 0.21			
	500°C, 50 dpa	10.4	$4.47 \pm 0.07$	0.56 ± 0.017	$3.24 \pm 0.41$
		<u>+</u> 0.49			
	500°C, 100 dpa	11.7	6.16 ± 0.70	$0.48 \pm 0.013$	1.93 ± 0.26
		± 0.33			

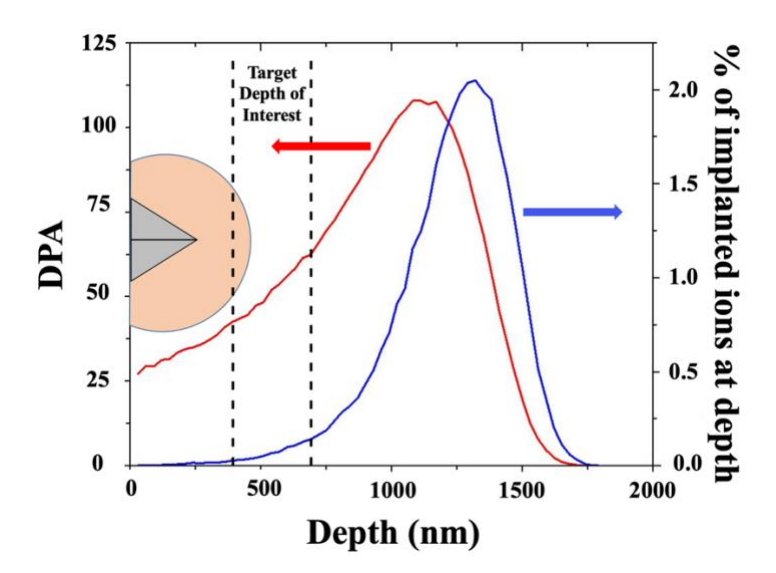


Figure 1: SRIM calculated damage profile, with the region of interest for microstructure characterization marked by dashed lines, and the plastic zone for top-down nanoindentation depicted.

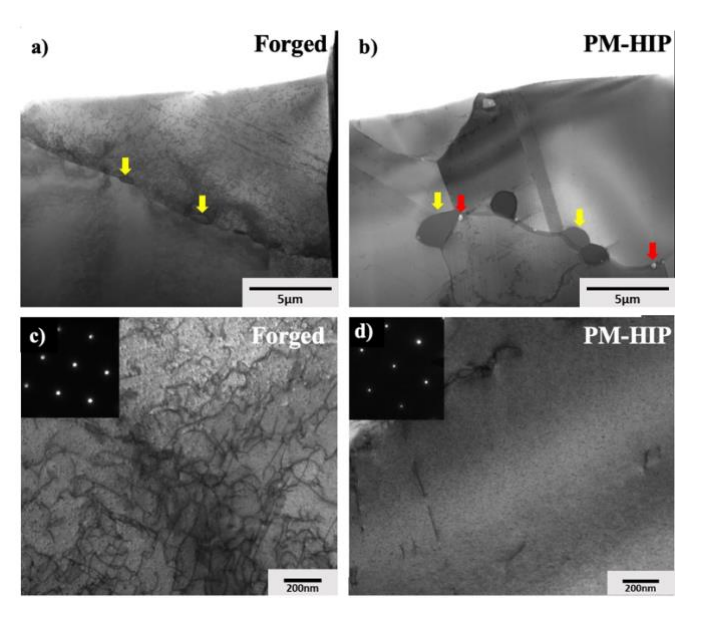


Figure 2: DZBFSTEM imaging of as-received microstructure illustrating (Nb,Mo)-rich carbides (yellow arrows) and oxide precipitates (red arrows) in a) forged and b) PM-HIP, and initial dislocation density in c) forged and d) PM-HIP.

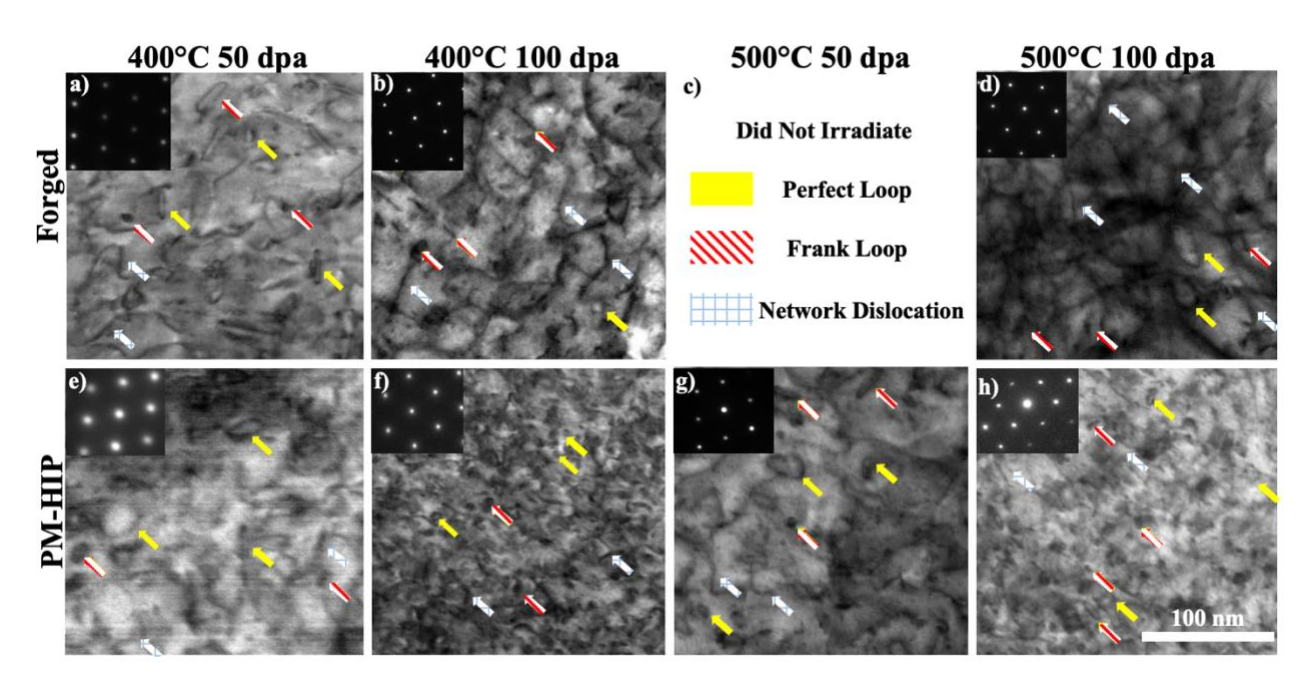


Figure 3: Representative DZBFSTEM micrographs taken along [110] zone axis showing dislocation loops and lines in a-d) forged and e-h) PM-HIP Alloy 625 under irradiation conditions of a,e) 400°C 50 dpa, b,f) 400°C 100 dpa, c,g) 500°C 50 dpa, d,h) 500°C 100 dpa.

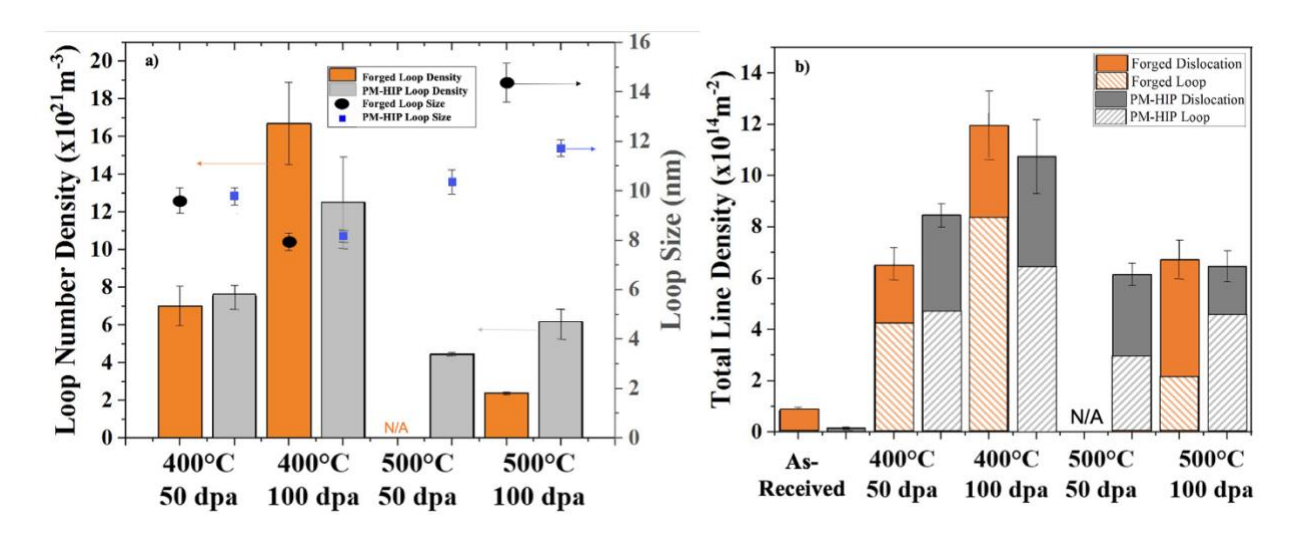


Figure 4: a) Effect of irradiation dose and temperature on dislocation loop size and number density; and b) total loop and line density.

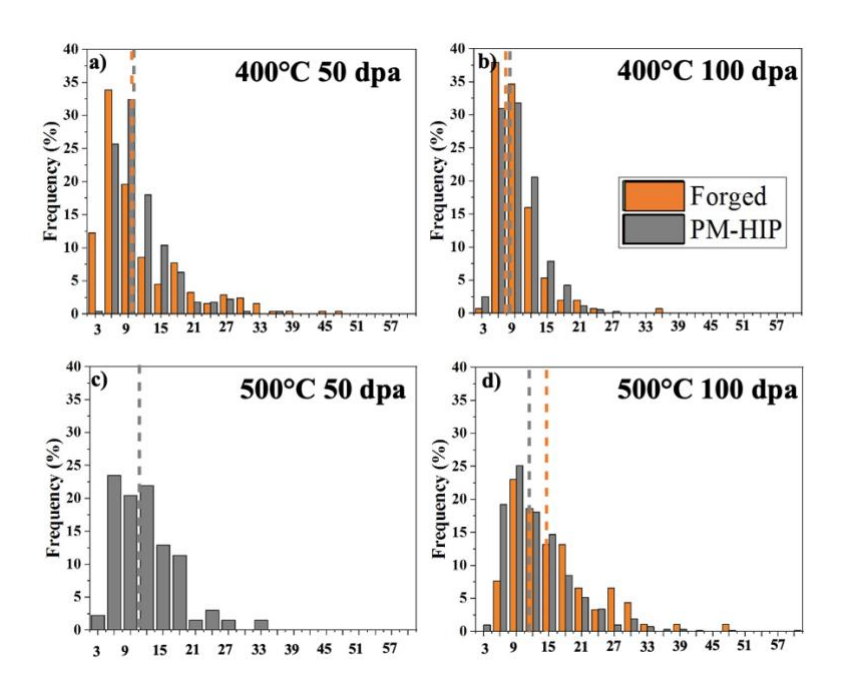


Figure 5: Loop size distribution histograms for a) 400°C 50 dpa, b) 400°C 100 dpa, c) 500°C 50 dpa, d) 500°C 100 dpa; vertical dashed lines indicate average loop diameter.

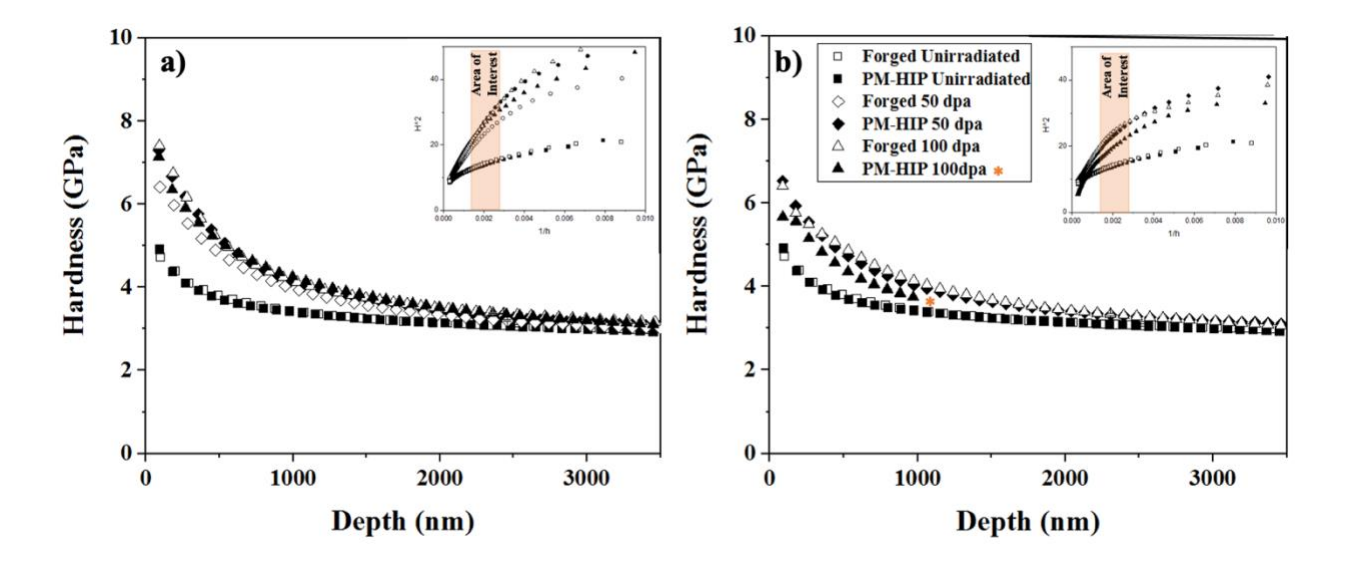


Figure 6: Average hardness-depth curves taken over 40+ top-down nanoindents in the a) 400°C b) 500°C conditions; insets show square of hardness against inverse of indent depth. Note that only the PM-HIP 500°C, 100 dpa (marked by \*) hardness-depth profile is taken from cross-sectional indents.

### References

- [1] X. Lou, D. Gandy, Advanced Manufacturing for Nuclear Energy, Jom. 71 (2019) 2834–2836. https://doi.org/10.1007/s11837-019-03607-4.
- [2] D.W. Gandy, PM-HIP research for structural and pressuring retaining applications within the electric power industry, 2015.
- [3] D.W. Gandy, J. Shingledecker, J. Siefert, Overcoming Barriers for Using PM/HIP Technology to Manufacture Large Power Generation Components PM/HIP opens up a new method of manufacturing high pressure-retaining components for use in the power-generation industry. (a) (b), Adv. Mater. Process. (2012).
- [4] H. V Atkinson, S. Davies, Fundamental Aspects of Hot Isostatic Pressing: An Overview, Metall. Mater. Trans. 31A (2000). https://link.springer.com/content/pdf/10.1007%2Fs11661-000-0078-2.pdf (accessed August 26, 2019).
- [5] European Powder Metallurgy Association, Introduction to PM HIP Technology, (n.d.). http://www.epma.com/pdfs/Final\_HIP\_Brochure\_Low\_res.pdf.
- [6] H.R. Dugdale, J.B. Borradaile, Development of hot isostatically pressed nickel based alloys for nuclear applications, Energy Mater. Mater. Sci. Eng. Energy Syst. 8 (2013) 374–381. https://doi.org/10.1179/1743290113Y.0000000076.
- [7] A. Kreitcberg, V. Brailovski, S. Turenne, Effect of heat treatment and hot isostatic pressing on the microstructure and mechanical properties of Inconel 625 alloy processed by laser powder bed fusion, Mater. Sci. Eng. A. 689 (2017) 1–10. https://doi.org/10.1016/j.msea.2017.02.038.
- [8] M.H. Bocanegra-Bernal, Review Hot Isostatic Pressing (HIP) technology and its

- applications to metals and ceramics, n.d.
- [9] D.P. Guillen, J.P. Wharry, D.W. Gandy, Ongoing irradiations of nuclear structural materials fabricated by powder metallurgy with hot isostatic pressing, Trans. Am. Nucl. Soc. 116 (2017) 392–393.
- [10] A. Lind, U. Bergenlid, Mechanical properties of hot isostatic pressed type 316LN steel after irradiation, J. Nucl. Mater. 283–287 (2000) 451–454. https://doi.org/10.1016/S0022-3115(00)00084-2.
- [11] L. Jiang, M. Song, L. Yang, J. Yang, D. Du, X. Lou, Y. Chen, A comparison study of void swelling in additively manufactured and cold-worked 316L stainless steels under ion irradiation, J. Nucl. Mater. 551 (2021) 152946.

  https://doi.org/10.1016/j.jnucmat.2021.152946.
- [12] L.J. Yu, E.A. Marquis, Precipitation behavior of Alloy 625 and Alloy 625 plus, J. Alloys Compd. 811 (2019) 151916. https://doi.org/10.1016/j.jallcom.2019.151916.
- [13] E. Getto, B. Tobie, E. Bautista, A.L. Bullens, Z.T. Kroll, M.J. Pavel, K.S. Mao, D.W. Gandy, J.P. Wharry, Thermal Aging and the Hall–Petch Relationship of PM-HIP and Wrought Alloy 625, Jom. 71 (2019) 2837–2845. https://doi.org/10.1007/s11837-019-03532-6.
- [14] P.P. Joshi, N. Kumar, K.L. Murty, Materials for Nuclear Reactors, Elsevier Ltd., 2020. https://doi.org/10.1016/b978-0-12-803581-8.12070-3.
- [15] A.F. Rowcliffe, L.K. Mansur, D.T. Hoelzer, R.K. Nanstad, Perspectives on radiation effects in nickel-base alloys for applications in advanced reactors, J. Nucl. Mater. 392 (2009) 341–352. https://doi.org/10.1016/j.jnucmat.2009.03.023.
- [16] G.S. Was, M. Song, M. Wang, IASCC Susceptibility and Evolution of Microstructure in

- Several Ni-Base Alloys after Proton Irradiation, 2015.
- [17] M. Wang, C. Lear, Proton Irradiation Screening Results of Select Advanced Replacement Alloys for Core Internals, 2017.
- [18] L. Yu, E.A. Marquis, Microstructural Responses of Alloy 625 and Alloy 625 Plus Under Ion and Proton Irradiations, JOM. (2020). https://doi.org/10.1007/s11837-020-04211-7.
- [19] M. Song, Y. Yang, M. Wang, W. Kuang, C.R. Lear, G.S. Was, Probing long-range ordering in nickel-base alloys with proton irradiation, Acta Mater. (2018). https://doi.org/10.1016/j.actamat.2018.06.043.
- [20] I. Cieślik, M. Duchna, T. Płociński, E. Wyszkowska, A. Azarov, M. Zieniuk, Ion irradiation effect on the microstructure of Inconel 625 obtained by Selective Laser Melting and by the metallurgical process, Surf. Coatings Technol. 396 (2020) 125952. https://doi.org/10.1016/j.surfcoat.2020.125952.
- [21] R. Bajaj, W.J. Mills, M.R. Lebo, B.Z. Hyatt, M.G. Burke, Irradiation-Assisted Stress Corrosion Cracking of HTH Alloy X-750 and Alloy 625, in: Int. Symp. Environ. Degrad. Mater. Nucl. Power Plants Water React., 1995.
- [22] D.P. Guillen, D.C. Pagan, E.M. Getto, J.P. Wharry, In situ tensile study of PM-HIP and wrought 316 L stainless steel and Inconel 625 alloys with high energy diffraction microscopy, Mater. Sci. Eng. A. 738 (2018) 380–388. https://doi.org/10.1016/j.msea.2018.09.083.
- [23] A. Bullens, K. Mao, E. Bautista, J. Wharry, Comparison of PM-HIP to Cast Alloy 625 for Nuclear Applications, in: n.d.
- [24] S. Floreen, G.E. Fuchs, W.J. Yang, The Metallurgy of Alloy 625, (2012) 13–37.https://doi.org/10.7449/1994/superalloys\_1994\_13\_37.

- [25] J.F. Ziegler, M.D. Ziegler, J.P. Biersack, SRIM The stopping and range of ions in matter (2010), Nucl. Instruments Methods Phys. Res. Sect. B Beam Interact. with Mater. Atoms. 268 (2010) 1818–1823. https://doi.org/10.1016/j.nimb.2010.02.091.
- [26] R.E. Stoller, M.B. Toloczko, G.S. Was, A.G. Certain, S. Dwaraknath, F.A. Garner, On the use of SRIM for computing radiation damage exposure, Nucl. Instruments Methods Phys. Res. B (2013) 75–80. https://doi.org/10.1016/j.nimb.2013.05.008.
- [27] P. Changizian, C. Lu, Z. Yao, L.M. Wang, Indentation behaviour of ion-irradiated X-750 Ni-based superalloy, Philos. Mag. Lett. 97 (2017) 101–109. https://doi.org/10.1080/09500839.2017.1288941.
- [28] H. Ken, Z. Yao, C. Judge, M. Griffiths, Microstructural evolution of CANDU spacer material Inconel X-750 under in situ ion irradiation, J. Nucl. Mater. 443 (2013) 49–58. https://doi.org/10.1016/j.jnucmat.2013.06.034.
- [29] S.J. Zinkle, L.L. Snead, Opportunities and limitations for ion beams in radiation effects studies: Bridging critical gaps between charged particle and neutron irradiations, Scr. Mater. 143 (2018) 154–160. https://doi.org/10.1016/j.scriptamat.2017.06.041.
- [30] L.A. Giannuzzi, J.L. Drown, S.R. Brown, R.B. Irwin, F.A. Stevie, Applications of the FIB lift-out technique for TEM specimen preparation., Microsc. Res. Tech. 41 (1998) 285–290. https://doi.org/10.1002/(SICI)1097-0029(19980515)41:4<285::AID-JEMT1>3.0.CO;2-Q.
- [31] B. Myers, TEM Sample Preparation with the FIB/SEM- NUANCE Center, 2009.
- [32] C.M. Parish, K.G. Field, A.G. Certain, J.P. Wharry, Application of STEM characterization for investigating radiation effects in BCC Fe-based alloys, J. Mater. Res. 30 (2015) 1275–1289. https://doi.org/10.1557/jmr.2015.32.

- [33] P. Xiu, Y.N. Osetsky, L. Jiang, G. Velisa, Y. Tong, H. Bei, W.J. Weber, Y. Zhang, L. Wang, Dislocation loop evolution and radiation hardening in nickel-based concentrated solid solution alloys, J. Nucl. Mater. 538 (2020) 152247.
  https://doi.org/10.1016/j.jnucmat.2020.152247.
- [34] K.G. Field, S.A. Briggs, K. Sridharan, Y. Yamamoto, R.H. Howard, Dislocation loop formation in model FeCrAl alloys after neutron irradiation below 1 dpa, J. Nucl. Mater. 495 (2017) 20–26. https://doi.org/10.1016/j.jnucmat.2017.07.061.
- [35] P. Xiu, H. Bei, Y. Zhang, L. Wang, K.G. Field, STEM Characterization of Dislocation Loops in Irradiated FCC Alloys, J. Nucl. Mater. 544 (2021) 152658. https://doi.org/10.1016/j.jnucmat.2020.152658.
- [36] X. Xiao, L. Yu, Nano-indentation of ion-irradiated nuclear structural materials: A review, Nucl. Mater. Energy. 22 (2020) 100721. https://doi.org/10.1016/j.nme.2019.100721.
- [37] P. Hosemann, D. Kiener, Y. Wang, S.A. Maloy, Issues to consider using nano indentation on shallow ion beam irradiated materials, J. Nucl. Mater. 425 (2012) 136–139. https://doi.org/10.1016/j.jnucmat.2011.11.070.
- [38] P. Hosemann, C. Vieh, R.R. Greco, S. Kabra, J.A. Valdez, M.J. Cappiello, S.A. Maloy, Nanoindentation on ion irradiated steels, J. Nucl. Mater. 389 (2009) 239–247. https://doi.org/10.1016/j.jnucmat.2009.02.026.
- [39] M. Saleh, Z. Zaidi, M. Ionescu, C. Hurt, K. Short, J. Daniels, P. Munroe, L. Edwards, D. Bhattacharyya, Relationship between damage and hardness profiles in ion irradiated SS316 using nanoindentation Experiments and modelling, Int. J. Plast. 86 (2016) 151–169. https://doi.org/10.1016/j.ijplas.2016.08.006.
- [40] M. Swenson, C.K. Dolph, J. Douglas, M.J. Swenson, J.P. Wharry, Plastic zone size for

- nanoindentation of irradiated Fe-9 % Cr ODS, J. Nucl. Mater. 481 (2016) 33–45. https://doi.org/10.1016/j.jnucmat.2016.08.033.
- [41] C. Heintze, F. Bergner, S. Akhmadaliev, E. Altstadt, Ion irradiation combined with nanoindentation as a screening test procedure for irradiation hardening, J. Nucl. Mater. 472 (2016) 196–205. https://doi.org/10.1016/j.jnucmat.2015.07.023.
- [42] M.A. Mattucci, I. Cherubin, P. Changizian, T. Skippon, M.R. Daymond, Indentation size effect, geometrically necessary dislocations and pile-up effects in hardness testing of irradiated nickel, Acta Mater. 207 (2021) 116702. https://doi.org/10.1016/j.actamat.2021.116702.
- [43] D.E.J. Armstrong, C.D. Hardie, J.S.K.L. Gibson, A.J. Bushby, P.D. Edmondson, S.G. Roberts, Small-scale characterisation of irradiated nuclear materials: Part II nanoindentation and micro-cantilever testing of ion irradiated nuclear materials, J. Nucl. Mater. 462 (2015) 374–381. https://doi.org/10.1016/j.jnucmat.2015.01.053.
- [44] Y. Gao, Y. Ding, J. Chen, J. Xu, Y. Ma, X. Wang, Effect of twin boundaries on the microstructure and mechanical properties of Inconel 625 alloy, Mater. Sci. Eng. A. 767 (2019) 138361. https://doi.org/10.1016/j.msea.2019.138361.
- [45] L. Tan, G. He, F. Liu, Y. Li, L. Jiang, Effects of temperature and pressure of hot isostatic pressing on the grain structure of powder metallurgy superalloy, Materials (Basel). 11 (2018). https://doi.org/10.3390/ma11020328.
- [46] C. Cai, X. Gao, Q. Teng, R. Kiran, J. Liu, Q. Wei, Y. Shi, Hot isostatic pressing of a near α-Ti alloy: Temperature optimization, microstructural evolution and mechanical performance evaluation, Mater. Sci. Eng. A. 802 (2021) 140426.

  https://doi.org/10.1016/j.msea.2020.140426.

- [47] T. Berglund, F. Meurling, Oxygen Content in PM HIP 625 and its Effect on Toughness,
   Hot Isostatic Press. HIP'17. 10 (2019) 135–141. https://doi.org/10.21741/9781644900031 19.
- [48] A. Sergi, R.H.U. Khan, M.M. Attallah, The role of powder atomisation route on the microstructure and mechanical properties of hot isostatically pressed Inconel 625, Mater. Sci. Eng. A. 808 (2021) 140950. https://doi.org/10.1016/j.msea.2021.140950.
- [49] J. Tucker, Modeling and Validation of Irradiation Damage in Ni-based Alloys for Long-Term LWR Applications, 2013.
- [50] M. Song, C.R. Lear, C.M. Parish, M. Wang, G.S. Was, Radiation tolerance of commercial and advanced alloys for core internals: a comprehensive microstructural characterization, J. Nucl. Mater. 510 (2018) 396–413. https://doi.org/10.1016/j.jnucmat.2018.08.035.
- [51] M. Wang, M. Song, C.R. Lear, G.S. Was, Irradiation assisted stress corrosion cracking of commercial and advanced alloys for light water reactor core internals, J. Nucl. Mater. 515 (2019) 52–70. https://doi.org/10.1016/j.jnucmat.2018.12.015.
- [52] G.S. Was, M. Song, M. Wang, Light Water Reactor Sustainability Program Assessment of Radiation Resistance of Selected Alloys in The ARRM Program Using Ion Irradiation, 2016.
- [53] C.J. Ulmer, A.T. Motta, Characterization of faulted dislocation loops and cavities in ion irradiated alloy 800H, J. Nucl. Mater. 498 (2018) 458–467.
  https://doi.org/10.1016/j.jnucmat.2017.11.012.
- [54] S.A. Briggs, C.M. Barr, J. Pakarinen, M. Mamivand, K. Hattar, D.D. Morgan, M. Taheri, K. Sridharan, Observations of defect structure evolution in proton and Ni ion irradiated Ni-Cr binary alloys, J. Nucl. Mater. (2016).

- https://doi.org/10.1016/j.jnucmat.2016.06.046.
- [55] S. Jin, X. He, T. Li, S. Ma, R. Tang, L. Guo, Microstructural evolution in nickel alloy C-276 after Ar-ion irradiation at elevated temperature, Mater. Charact. 72 (2012) 8–14. https://doi.org/10.1016/j.matchar.2012.06.010.
- [56] R.M. Boothby, Radiation effects in nickel-based alloys, Elsevier Inc., 2012. https://doi.org/10.1016/B978-0-08-056033-5.00090-2.
- [57] G.S. WAS, G.S. Was, Fundamentals of Radiation Materials Science, 2017. https://doi.org/10.1007/978-1-4939-3438-6\_1.
- [58] S. Zhao, G.M. Stocks, Y. Zhang, Stacking fault energies of face-centered cubic concentrated solid solution alloys, Acta Mater. 134 (2017) 334–345. https://doi.org/10.1016/j.actamat.2017.05.001.
- [59] Y. Dou, H. Luo, Y. Jiang, X. Tang, Effects of alloying elements on the stacking fault energies of Ni58Cr32Fe10 alloys: A first-principle study, Metals (Basel). 9 (2019) 1–9. https://doi.org/10.3390/met9111163.
- [60] H.K. Zhang, Z. Yao, M.R. Daymond, M.A. Kirk, Elevated temperature irradiation damage in CANDU spacer material Inconel X-750, J. Nucl. Mater. (2013). https://doi.org/10.1016/j.jnucmat.2013.11.008.
- [61] C. Sun, M. Kirk, M. Li, K. Hattar, Y. Wang, O. Anderoglu, J. Valdez, B.P. Uberuaga, R. Dickerson, S.A. Maloy, Microstructure, chemistry and mechanical properties of Ni-based superalloy Rene N4 under irradiation at room temperature, Acta Mater. 95 (2015) 357–365. https://doi.org/10.1016/j.actamat.2015.04.061.
- [62] L.M. Wang, R.A. Dodd, G.L. Kulcinski, Effects of 14 MeV nickel ion irradiation on nickel-copper alloys observed in cross-section, J. Nucl. Mater. 155–157 (1988) 1241–

- 1248. https://doi.org/10.1016/0022-3115(88)90504-1.
- [63] Y. Bazarbayev, M. Kattoura, K.S. Mao, J. Song, V.K. Vasudevan, J.P. Wharry, Effects of corrosion-inhibiting surface treatments on irradiated microstructure development in Ni-base alloy 718, J. Nucl. Mater. 512 (2018) 276–287.
  https://doi.org/10.1016/j.jnucmat.2018.10.006.
- [64] S. Jin, L. Guo, Y. Ren, R. Tang, Y. Qiao, TEM Characterization of Self-ion Irradiation Damage in Nickel-base Alloy C-276 at Elevated Temperature, J. Mater. Sci. Technol. 28 (2012) 1039–1045. https://doi.org/10.1016/S1005-0302(12)60170-4.
- [65] J.. Horak, A.F. Rowcliffe, Tensile Properties and Fracture Behavior of Irradiated Nickel Alloys, in: Trans. Am. Nucl. Soc., 1981.
- [66] S.J. Zinkle, P.J. Maziasz, R.E. Stoller, Dose dependence of the microstructural evolution in neutron-irradiated austenitic stainless steel, J. Nucl. Mater. 206 (1993) 266–286. https://doi.org/10.1016/0022-3115(93)90128-L.
- [67] G.S. Was, Fundamentals of Radiation Material Science Ch. 7 Dislocation Microstructure, 2017. https://doi.org/10.1007/978-1-4939-3438-6.
- [68] D.S. Gelles, A Frank Loop Unfaulting Mechanism in FCC Metals During Neutron Irradiation, in: 1980.
- [69] M. Suzuki, A. Sato, T. Mori, J. Nagakawa, N. Yamamoto, H. Shiraishi, In situ deformation and unfaulting of interstitial loops in proton-irradiated steels, Philos. Mag. A Phys. Condens. Matter, Struct. Defects Mech. Prop. 65 (1992) 1309–1326. https://doi.org/10.1080/01418619208205606.
- [70] H. Wiedersich, On the theory of void formation during irradiation, Radiat. Eff. 12 (1972) 111–125. https://doi.org/10.1080/00337577208231128.

- [71] A. Brailsford, The Theory of Sink Strengths, Proc. Roy. Soc. 302 A (1981) 87.
- [72] K. Ma, B. Décamps, A. Fraczkiewicz, F. Prima, M. Loyer-Prost, Drastic influence of micro-alloying on Frank loop nature in Ni and Ni-based model alloys, 8 (2020) 201–207. https://doi.org/10.1080/21663831.2020.1741042.
- [73] A. Hoffman, L. He, M. Luebbe, H. Pommerenke, J. Duan, P. Cao, K. Sridharan, Z. Lu, H. Wen, Effects of Al and Ti Additions on Irradiation Behavior of FeMnNiCr Multi-Principal-Element Alloy, Jom. 72 (2020) 150–159. https://doi.org/10.1007/s11837-019-03871-4.
- [74] T. Yoshiie, Q. Xu, Effects of alloying elements Mn, Mo, Ti, Si, P and C on the incubation period of void swelling in austenitic stainless steels, Tungsten. 3 (2021) 3–19. https://doi.org/10.1007/s42864-021-00077-7.
- [75] R. Sizmann, The effect of radiation upon diffusion in metals, J. Nucl. Mater. 69–70 (1978) 386–412. https://doi.org/10.1016/0022-3115(78)90256-8.
- [76] I.J. Beyerlein, A. Caro, M.J. Demkowicz, N.A. Mara, A. Misra, B.P. Uberuaga, Radiation damage tolerant nanomaterials, Mater. Today. 16 (2013) 443–449.
  https://doi.org/10.1016/j.mattod.2013.10.019.
- [77] G. Ackland, Controlling Radiation Damage, Sci. Mag. 327 (2010). https://doi.org/10.1126/science.1185988.
- [78] J. Li, C. Fan, J. Ding, S. Xue, Y. Chen, Q. Li, H. Wang, X. Zhang, In situ heavy ion irradiation studies of nanopore shrinkage and enhanced radiation tolerance of nanoporous Au, Sci. Rep. 7 (2017) 1–10. https://doi.org/10.1038/srep39484.
- [79] J.G. Gigax, H. Kim, T. Chen, F.A. Garner, L. Shao, Radiation instability of equal channel angular extruded T91 at ultra-high damage levels, Acta Mater. 132 (2017) 395–404.

- https://doi.org/10.1016/j.actamat.2017.04.038.
- [80] T. Chen, E. Aydogan, J.G. Gigax, D. Chen, J. Wang, X. Wang, S. Ukai, F.A. Garner, L. Shao, Microstructural changes and void swelling of a 12Cr ODS ferritic-martensitic alloy after high-dpa self-ion irradiation, J. Nucl. Mater. 467 (2015) 42–49. https://doi.org/10.1016/j.jnucmat.2015.09.016.